International Journal of Legal Medicine
https://doi.org/10.1007/s00414-024-03396-9

ORIGINAL ARTICLE

Exploring radiomic features of lateral cerebral ventricles in postmortem CT for postmortem interval estimation

Fabio De-Giorgio[1,2] · Michele Guerreri[3] · Roberto Gatta[3] · Eva Bergamin[1,2] · Vittorio De Vita[1,2] · Matteo Mancino[1,4] · Luca Boldrini[1,4] · Evis Sala[1,4] · Vincenzo L. Pascali[1,2]

Received: 5 October 2024 / Accepted: 8 December 2024

Abstract
The aim of this study is to investigate the potential of radiomic features extracted from postmortem computed tomography (PMCT) scans of the lateral cerebral ventricles (LCVs) to provide information on the time since death, or postmortem interval (PMI), a critical aspect of forensic medicine. Periodic PMCT scans, referred to as "sequential scans", were obtained from twelve corpses with known times of death, ranging from 5.5 to 273 h postmortem. Radiomics features were then extracted from the LCVs, and a mixed-effect model, specifically designed for sequential data, was employed to assess the association between feature values and PMI. Four model variants were fitted to the data to identify the best functional form to explain the relationship between the variables. Significant associations were observed for features, the most significant being the median Hounsfield Units (HU) within the LCVs ($p < 9.47 \times 10^{-9}$), LCVs surface area ($p < 4.69 \times 10^{-6}$), L-major axis ($p < 2.17 \times 10^{-5}$), L-minor axis ($p < 1.30 \times 10^{-4}$), and HU entropy ($p < 4.16 \times 10^{-4}$). Our findings align with previous studies, supporting a logarithmic model for PMI-related changes in LCV volume and mean HU intensity value. This study highlights the potential of PMCT-based radiomics as source of complementary information that could be integrated into existing methods for PMI estimation. Our results support the application of a quantitative imaging approach in forensic investigations.

Keywords Postmortem interval · Time of death · Postmortem computed tomography · Lateral cerebral ventricle · Radiomics · Radiomic features

Introduction

Estimating the postmortem interval (PMI) is a crucial aspect of forensic medicine, aiming to precisely determine the time elapsed between death and the discovery of the body. This data is essential for guiding criminal investigations and providing information to law enforcement [1–3]. The complexity of PMI estimation arises from numerous factors affecting body changes after death, including the cause of death, environmental conditions (i.e., external temperature and body location), and individual characteristics (i.e., body mass, temperature, age, and gender) [4].

Over the years, various approaches have been developed to address this challenge, utilizing different parameters and techniques based on the body's condition. In early postmortem periods, parameters deriving from physical and physicochemical processes are often used, while alternative techniques, such as forensic entomology or decomposition morphology classification, become more informative as the body undergoes advanced decomposition [1, 2, 5–13]. As new methods are developed, different parameters can be integrated into established techniques to create more complex models [12, 14], resulting in more reliable and precise estimates of the time of death [15, 16]. Hence, the search for new methods in the field is ongoing [17–21].

The use of imaging techniques in death investigations has a long-established history [22, 23], with postmortem

✉ Fabio De-Giorgio
fabio.degiorgio@unicatt.it

1 Fondazione Policlinico Universitario A. Gemelli IRCCS, Rome, Italy

2 Department of Healthcare Surveillance and Bioethics, Section of Legal Medicine, Università Cattolica del Sacro Cuore, Rome, Italy

3 Dipartimento di Scienze Cliniche e Sperimentali, Università degli Studi di Brescia, Brescia, Italy

4 Department of Diagnostic Imaging, Oncological Radiotherapy and Hematology, Università Cattolica del Sacro Cuore, Rome, Italy

Published online: 20 December 2024

computed tomography (PMCT) emerging as a standard practice, offering non-invasive alternatives to traditional autopsies [24–27]. However, while various postmortem changes observable through PMCT have been reported in different organs and body regions [28–31], the extent to which this information can be exploited to develop new PMI estimation methods remains largely unexplored.

Recent advancements in computing performance, reconstruction software, image processing, and data storage have expanded the applicability of Machine Learning (ML) algorithms for image analysis. In the medical imaging domain, radiomics has emerged as a popular approach [32], emphasizing that "images are more than pictures; they are data" [33]. Radiomics aims to develop automated and reproducible analysis methodologies, extracting previously inaccessible measurable attributes, known as features (i.e., shape, texture, or intensity), from images to provide objective information for analysis [32]. Initially designed to improve diagnosis, prognosis, and treatment planning in the field of oncology [34–43], radiomics has quickly proven to be applicable in broader contexts [44–48].

Specifically, in the context of PMI estimation, the information extracted from PMCT images using a radiomic-based approach could be used to improve the reliability and precision of estimates. However, despite the undeniable potential of radiomics applied to PMCT [49], only a limited number of studies utilizing such an approach can be found in the literature. De-Giorgio et al. [50] used fractal analysis on sequential CT scans (multiple scans at different time points) of four subjects to characterize brain postmortem changes. Klontzas et al. [51] constructed a predictive model that combines conventional IBSI-compliant radiomic features [52] from both the pancreas and liver to predict the PMI. The model was trained and tested using cross-sectional data, with a single scan available for each of the subjects included in the analysis. Given its potential, radiomics applied to PMCT could leverage extensive data from various organs to significantly enhance forensic and medical insights.

In this framework, the lateral cerebral ventricles (LCVs) have been observed to undergo significant postmortem modifications visible on PMCT that might be useful for PMI determination [29, 53]. Hasegawa et al. [54] analysed sequential CT scans of three corpses in the range of 0–24 h postmortem and observed an increase in the average Hounsfield units (HU) of the cerebrospinal fluid within the LCVs, as well as a decrease in the volume of the ventricles over time. De-Giorgio et al. [55] confirmed these results using a larger cohort (ten corpses), as well as a wider range of PMIs (ranging from ~5.5–273 h postmortem). In addition, the authors showed that the HU changed in a logarithmic fashion, with a steeper increase at low PMIs that reduced as the PMI increased. While these results are promising, they constitute only a minimal part of the information that can be extracted through radiomics.

The aim of this work is to demonstrate how radiomic analysis can extract valuable information to complement current PMI estimation approaches. We chose the LCVs, which have been shown to undergo relevant changes after death that can be quantified via PMCT. We analysed twelve bodies that were sequentially scanned over a range of 4.5–219 h postmortem. We extracted IBSI-compliant radiomic features [52] from the LCVs and assessed whether there is a statistically significant association between these radiomic features and the PMI, using a model well-suited for sequential data. Additionally, we investigated different types of functional associations.

Materials and methods

Subject recruitment and CT measurements

The research retrospectively included bodies that arrived at our Forensic Medicine Institute between May 2021 and May 2022. A total of 12 subjects were included in the study, with a mean age at the time of death of 62.5 years (age range = 23–86 years; SD = 18.7). Of the 12 subjects, 2 were females and 10 were males (Table 1). Inclusion criteria were a known time of death (presence of witnesses) and age above 18 years. Exclusion criteria comprised the presence of clinically and/or radiologically significant brain pathologies and/or brain traumatic lesions. All bodies were transferred to our Institute within 6 h from death. Upon arrival, the clothes were removed, and the corpses were positioned horizontally on the CT table within the CT room, in the supine position with their arms at their sides and wrapped in body bags. The corpses were kept in the same position throughout the entire procedure and remained in the CT room for the entire series acquisition, at a controlled temperature of 20 °C and air humidity of 49%.

Each corpse underwent a variable number of sequential CT scans before autopsy, with a total of 72 CT scans and an average of 6 scans (number of scans range = 3–14, SD = 3.7) per subject. Each acquisition was performed at different PMIs. The average PMI acquisition time was 31.8 h postmortem (PMI range = 4.5–219 h, SD = 35.3). The average PMI at which the first scan was performed was 13.1 h postmortem (first scan PMI range = 4.1–32.8, SD = 10.2). All CT examinations were conducted on a Somatom Scope 16-slice CT scanner, Siemens Healthineers Italia, using the following parameters: 130 kV, 150 mA, 2.4-mm slice thickness, H31S head-district kernel reconstruction. Cranial CT scans from the skull vertex to the sternal notch (1-mm reconstructions) were acquired. No contrast agent was used in this

Table 1 A comprehensive list of the studied cases, including baseline parameters (gender, age), cause of death, and postmortem interval (PMI) at first and last postmortem computed tomography (PMCT) scan

Case	Gender	Age	Cause of death	PMI at first PMCT scan (hours)	PMI at last PMCT scan (hours)
1	**F**	**78**	Sudden cardiac death	6,85	19,05
2	**M**	**83**	Sudden cardiac death	26,42	50,43
3	**M**	**58**	Frostbite in subject with pneumonia	16,18	108,90
4	**M**	**86**	Sudden cardiac death	4,72	42,82
5	**M**	**75**	Acute respiratory failure	5,48	19,32
6	**M**	**55**	Sudden cardiac death	5,67	9,17
7	**M**	**78**	Sudden cardiac death	7,18	9,87
8	**M**	**61**	Sudden cardiac death	4,18	12,02
9	**M**	**23**	Sudden cardiac death	22,02	80,83
10	**M**	**62**	Sudden cardiac death	21,53	73,53
11	**F**	**49**	Sepsis	32,82	219,27
12	**M**	**42**	Suicidal death from slaughter	4,50	49,00

procedure. Scans were then evaluated by a senior radiologist to ensure reliability and quality, and repeated in case of artifacts. Following CT analysis, all corpses underwent autopsy and standard histological/toxicological analyses. All investigations (PMCT examination, autopsy, histological/toxicological analyses) were authorized by the Judicial Authority.

Image segmentation

An experienced neuroradiologist imported the PMCT series of each subject in DICOM format files using the 3D Slicer platform (https://www.slicer.org), v5.4.0 [56]. A region of interest (ROI) was drawn by manually contouring the LCVs for each subject timepoint (Fig. 1). The segmentation was performed primarily on axial scans, as

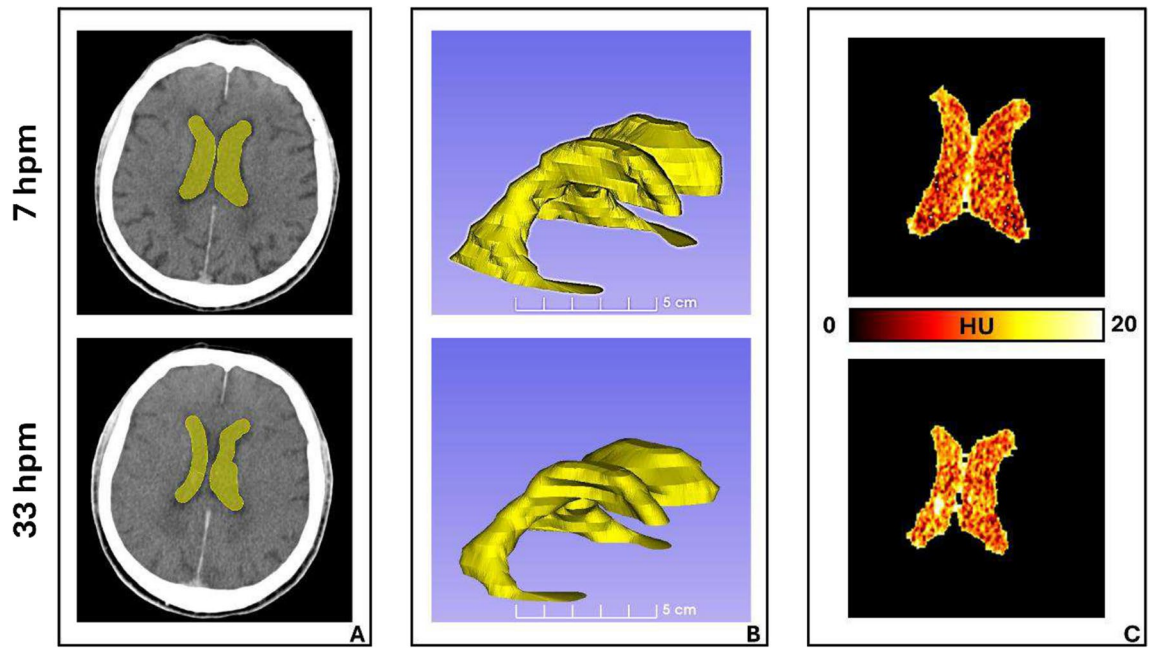

Fig. 1 Lateral cerebral ventricles (LCVs) segmentation and postmortem changes. We report the segmentation and visualization of the LCVs at two different postmortem time points for a representative subject. The presented scans have been acquired at about 7- and 33-hours postmortem (hpm). **A** shows an axial section of the two CT images with the corresponding segmentations of the LCVs overlayed in yellow. **B** shows a 3D rendering of the LCVs segmentations. The volume of the LCVs appears to decrease as the postmortem interval (PMI) increases. **C** shows the values of the Hounsfield units (HU) from the CT acquisitions within the LCVs. The intensity appears to increase as the PMI increases

they provide the most reliable resolution for this region, while the coronal and sagittal views were used to cross-check and refine the segmentation when necessary. The ROIs were then exported into an RTSTRUCT file format via the SlicerRT plug-in (v4.1.1).

Radiomics feature extraction

The IBSI-compliant software MODDICOM [57] implemented in R (v4.3.0) was used for the extraction of radiomic features from PMCT images. Features were extracted specifically from the manually segmented regions of interest (ROIs) corresponding to the lateral cerebral ventricles (LCVs). This approach ensures that the analysis focuses on the targeted anatomical structures, excluding surrounding tissues that could introduce bias and noise into the feature extraction process. A total of 117 features were extracted from the LCVs. This set of features included first-order statistics features (21), shape-based 3D features (14), and second-order statistics features (82). The latter can be further divided into grey level co-occurrence matrix (GLCM) features (50) and grey level size zone matrix (GLSZM) features (32). GLCM and GLSZM features included feature versions computed 2D (i.e. separately on each slice and then averaged across the slices), and features computed on 2.5D, an approach that attempts to integrate the information over multiple slices [52].

Statistical methods

To assess whether any of the extracted radiomic features could be used for PMI estimation, we computed the degree of association between the features and the PMI. Previous studies focusing on how the HU and the volume of LCVs vary with time postmortem [54, 55] performed this assessment separately for each of the subjects. In this work, we opted for an approach based on a mixed-effects model. This model is more appropriate for our dataset composed of sequential scans, as it can effectively handle the hierarchical structure of the data where multiple observations (time points) are nested within subjects. The mixed model that we used was defined as follows:

$$feature_f(PMI) + (1|subject) \quad (1)$$

In this model, the dependent variable is one of the extracted radiomic features, while the independent variable is a function of the PMI, f(PMI). The last part of the equation indicates that we use a random intercept, while the slope is considered as fixed effect. By including the random intercepts, this mixed-effects model accommodates the within-subject variability, providing a more accurate understanding of the association between features and PMI, while considering the repeated measures nature of the data. The use of a generic function of the PMI allows to model the relationship between variables without limiting it to a simple linear association. For example, the logarithmic trend observed by DeGiorgio et al. [55] between mean HU values and the PMI can be modelled with this approach setting $f(\text{PMI}) = ln(\text{PMI})$. The statistical analyses were performed with the software package R (v4.1.0). The mixed-effects model fit was performed using the *lmer* function of package *lme4* (v1.1–35.3).

Experiments

We aimed to select a subset of radiomic features strongly associated with the PMI and that could, therefore, potentially be used as predictors for PMI estimation. For each of the extracted features we fitted four different variants of the model described in the Eq. (1). The model variants differ in the definition of the function f(PMI). We used the following options: $f(\text{PMI}) = \text{PMI}, \text{PMI}^2, \text{PMI}^{1/2}, \ln(\text{PMI})$. The statistical significance of the association between the f(PMI) and the features was assessed via a t-test, evaluating whether the fixed effect coefficients (slopes) were significantly different from zero. To account for the multiple comparisons, the p-values obtained by fitting each variant of the four models to the data were adjusted using the false discovery rate (FDR) method. The adjusted p-values were considered significant when smaller than 0.05.

To understand which of the model variants was the most appropriate to explain the association between each of the features and the PMI, we estimated the model fitting performance in terms of quality of the fit. Specifically, the log-likelihood of the fitted models was used.

After identifying the set of features with a statistically significant association with the PMI, we performed an additional feature selection step to discard features that showed strong correlations with each other. This process ensured that we retained only those features that provided unique information. This step was performed by assessing the linear correlation between the selected features, pairwise. For each pair, if the correlation coefficient was greater than 0.7, the feature with the lowest degree of association with the PMI in terms of p-value was discarded.

Results

A total of 468 models (117 features × 4 model variants) were fitted to the data. We found a statistically significant association between radiomic feature and the PMI for 106 of these models. There were 37 different features that showed a statistically significant association for at least one of the model variants. Of these, 8 were first-order statistics features, 10

Table 2 Feature selection results. The features retained after the feature selection process are reported in the table. In addition, the table reports the class type the feature belongs to (first-level statistical, second-level statistical, shape-based), the model variant which gave the best results in terms of fit performance (simple linear, logarithmic, square-root), the p-value obtained testing whether the model fixed effect was different from zero, the fit performance in terms of the log-likelihood (Log-like), the conditional R2 of the model and the fixed effect obtained from the fit. SAHGLE 2.5D = 2.5D Small Area High Gray Level Emphasis; IDM 2.5D = 2.5D Inverse Difference Moment. Clust. Tend. = Cluster Tendency

Name	Feature Class	Model Variant	*p*-val	Log-like	Cond R^2	Fixed Eff	Std Err
Median	1st Lev. Stat.	Log	9.47E-09	−149.46	0.97	2.68E+00	3.29E-01
Surface	Shape-Based	Log	4.69E-06	−627.79	0.89	−1.33E+03	1.97E+02
L-major	Shape-Based	Lin	2.17E-05	−243.08	0.85	−1.74E-01	2.85E-02
L-minor	Shape-Based	Lin	1.30E-04	−195.18	0.97	−7.03E-02	1.25E-02
10th Percentile	1st Lev. Stat.	Log	3.68E-04	−172.83	0.96	2.27E+00	4.70E-01
Entropy	1st Lev. Stat.	Sqrt	4.16E-04	−12.13	0.81	8.42E-02	1.66E-02
SAHGLE 2.5D	2nd Lev. Stat.	Sqrt	1.10E-02	−432.13	0.90	2.36E+01	6.29E+00
IDM 2.5D	2nd Lev. Stat.	Sqrt	2.29E-02	226.40	0.74	−1.77E-03	7.09E+00
Clust. Tend. 2.5D	2nd Lev. Stat.	Sqrt	2.29E-02	−437.07	0.76	−2.31E+01	5.68E-04
Skewness	1st Lev. Stat.	Log	2.61E-02	−161.84	0.90	−1.30E+00	3.42E-01
Compactness (2)	Shape-Based	Lin	2.90E-02	203.18	0.89	1.47E-04	4.77E-05
Elongation	Shape-Based	Lin	4.86E-02	99.03	0.88	6.07E-04	2.16E-04

were shape-based features, 12 were GLCM features, and 7 were GLSZM features. Table 2 reports the results of the feature selection in which we discarded the features with high correlations, retaining only those that exhibit exclusive information about the processes that the LCVs undergo as the PMI increases. Of the 37 features found in the previous step, only 12 were retained. Of these, 4 were first-order statistics features, 5 were shape-based features, 2 were GLCM features, and 1 was a GLSZM feature.

Among the retained features, those with the strongest association with the PMI in terms of p-value were the median HU value within the LCVs, which increased with the PMI ($p < 1e\text{-}8$); the surface area of the LCVs, which decreased with the PMI ($p < 5e\text{-}6$); L-major and L-minor, the largest and second-largest axes length of the ROI-enclosing ellipsoid, which both decreased with the PMI ($p < 1e\text{-}4$ and $p < 1e\text{-}3$, respectively); the 10th percentile of the HU in the LCVs ($p < 1e\text{-}3$) and HU entropy, which measures the uncertainty/randomness of the HU values ($p < 1e\text{-}3$), which both increased with the PMI. Other significant features were: the 2.5D Small Area High Gray Level Emphasis (SAHGLE), which measures the proportion of smaller size zones with higher grey-level values in the image of the joint distribution; the 2.5D Inverse Difference Moment (IDM), a measure of the local homogeneity of the image; the 2.5D Cluster Tendency, a measure of groupings of voxels with similar grey-level values; the skewness of HU values; the type 2 compactness, a measure of how closely the shape of the ventricles approximates a sphere; the elongation, which indicates the relationship between the two largest principal components in the ROI shape.

For each of the selected features, Table 2 also reports the model variant which provided the best fit performance, i.e. the model variant with the highest log-likelihood. For all shape-based features, except for the LCVs surface area, a perfect linear relationship best described the data. A logarithmic relation best described all the first-order statistics features, except for the entropy. All the second-order statistics features were best described by a square-root relationship between the feature and the PMI. In none of the cases was the quadratic relationship between features and PMI found to be the most appropriate.

Figure 2 depicts three examples illustrating the plotting of feature values against the PMI. Each example represents a case where one of the model variants performed the best. In these plots, data points are represented as dots, with data from the same subject sharing the same colour and connected by dashed lines. Additionally, the plots include fitted models represented by solid lines. The number of lines corresponds to the number of subjects included in the study, with each line coloured consistently with the corresponding subject. These plots demonstrate how the model accounts for inter-subject variability through the random effect (the model intercepts), while the overall variation of the feature values as a function of the PMI value is accounted for by the fixed effect (the slope of the curves).

Table 3 reports the same information as Table 2, but for the mean HU of the LCVs, as well as for the ventricle's volume. These two features were previously reported having a significant correlation with PMI [54, 55]. In this study, both features were found to have a significant association with the PMI ($p < 0.01e\text{-}6$ and $p < 0.05e\text{-}5$, respectively), and were included in the initially selected 37

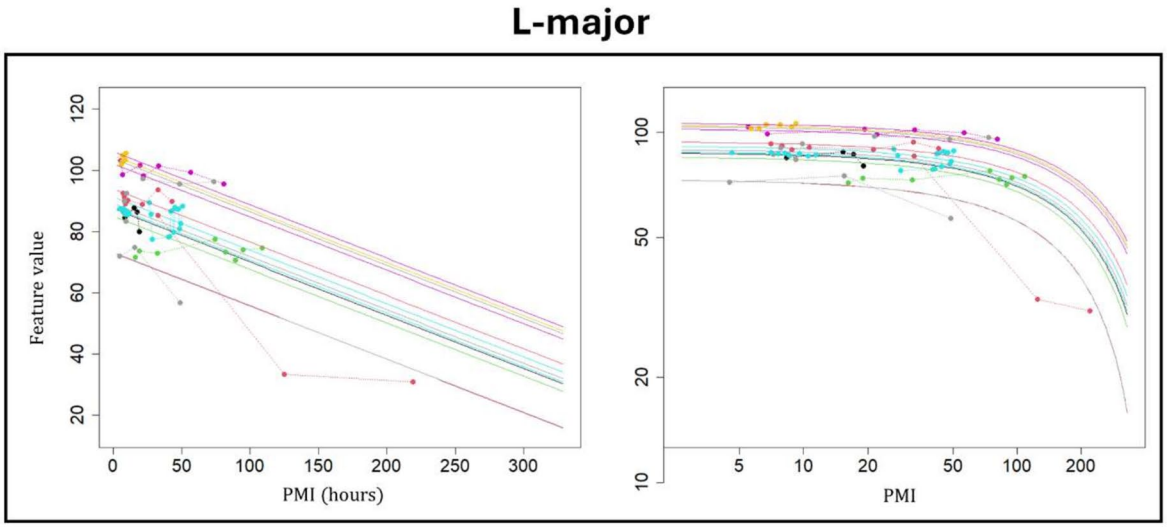
L-major
Feature value
PMI (hours)
PMI

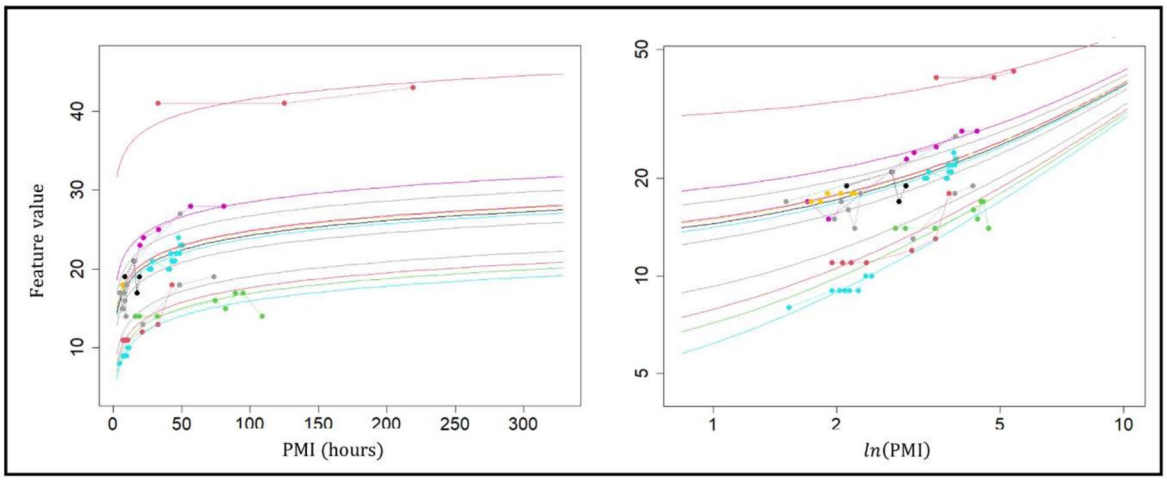
Median
Feature value
PMI (hours)
ln(PMI)

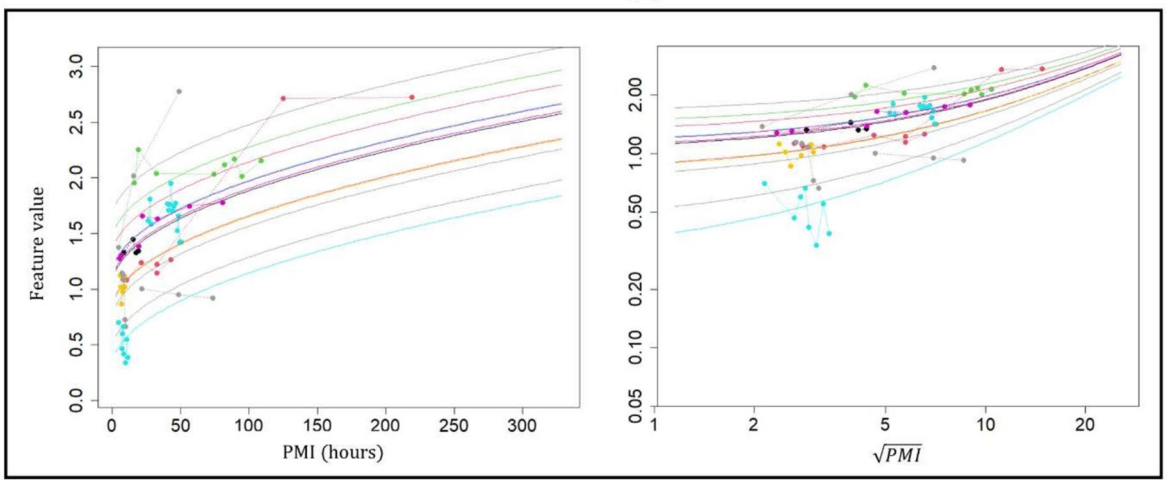
Entropy
Feature value
PMI (hours)
√PMI

◂**Fig. 2** Radiomic features vs. PMI plots. The figure shows the association between some representative radiomic features extracted from the lateral cerebral ventricles (LCVs) and the postmortem interval (PMI) expressed in hours. Three features are reported: the L-minor, the median of the LCVs intensities and their entropy. The features are exemplar of the model variants used to fit the data. The L-major was best represented by a perfect linear relationship with the PMI, the median had a logarithmic trend, while the entropy had a squared-root association with the PMI. For each feature we report two plots: on the left we plot the feature value as a function of the PMI, to show the different trends; on the right, we report the feature values as a function of *f*(PMI), where *f*(x) is equal to x, ln(x), and sqrt(x), respectively. Furthermore, in this latter plot we use log-scale axes to improve the data readability. In each plot, the data from the same subjects have same colours and are connected by dashed lines. The solid lines represent the fitted models. Different lines correspond to the different random effects estimated by the model, while the slope (the fixed effect) is shared by the subjects

features. However, they were excluded from the features reported in Table 2 as they exhibited strong correlations with other features, but weaker statistical significance. In both cases we found that the best model variant was the one assuming a logarithmic relation between the variables (Fig. 3).

Discussion

In the present study we identified several features extracted from the LCVs that exhibit a strong correlation with the PMI. This finding suggests that these features can effectively detect and quantify subtle changes occurring postmortem and highlights the potential that PMCT-based radiomics to positively impact the development of novel techniques for determining the PMI.

The feature that showed the strongest association with the PMI was the median of the PMCT intensity, computed within the LCVs. The increase in mean HU values over time after death has been previously reported and is associated to various postmortem mechanisms, such as CSF proteins and/or ependymal layer decomposition, CSF condensation, and the inflow of protein-like substances from the periventricular brain tissues into the CSF [54]. Compared to the mean, the median has the advantage of being more robust to outlier values. As already observed by De-Giorgio et al. [55], the logarithmic function used to fit the data diverges for infinite times. This is not physically meaningful and a saturation to approximately 40–50 HU, corresponding to the grey matter values, is expected at very long times. The increase of 10th percentile feature is in line with the increase in HU values, suggesting that the variation is mainly driven by the lowest value of the distribution. The positive correlation between entropy and PMI indicates greater complexity and heterogeneity in the texture of the LCVs postmortem, while the skewness decrease suggests that the distribution of the intensities tends to become more symmetric with respect to the centre of the distribution.

We found a strong correlation between the PMI and different shape-based features. These results are consistent with those previously reported, indicating a decrease in the overall LCVs volume over time after death [54, 55]. This process has been associated with the swelling of the brain soon after death, as well as with the softening of the brain and subsequent settling in the most gravity-dependent portions of the skull at more advanced decomposition stages [28, 29, 53, 54]. While the process is known, our results provide a more detailed understanding of the underlying mechanisms involved: first, we found that the surface area of LCVs is the most sensitive shape-based indicator of variations with the PMI. Furthermore, we found that morphological changes are mainly driven by the L-major, which represents the largest axis length of the ROI-enclosing ellipsoid. In the context of the ventricles, this axis can be considered to lay on the anterior-posterior head direction, with a good approximation. Hence, our results show that, in our cohort, the postmortem LCVs' shrinkage is mainly driven by an antero-posterior reduction of the ventricles. Since all our subjects were placed in the supine position, it is reasonable to assume that this is the effect of the brain settling in the most gravity-dependent portions of the skull. The PMI-related increase in compactness confirms this hypothesis, while the increase in elongation reflects the differential variation of the L-major and L-minor.

Our results are consistent with those previously reported in the literature [54, 55]. We observed a decrease in the volume of the LCVs, while the mean intensity value registered within the ventricles tended to increase. As already reported by De-Giorgio et al. [55], we found that the association between mean intensity and PMI was best described by a logarithmic function. The linear slope (using a logarithmic scale) we estimated (2.53 +/- 0.37) was slightly lower than the one reported by De-Giorgio et al. (3.91 +/- 0.19), but the two results are comparable. The difference could be due to the different approach used to fit the data. We found that the relationship between LCVs' volume and PMI was best described by a logarithmic function, whereas previous reports used a simple linear function.

While the changes detected and reported in this paper show that a radiomic-based analysis of the LCVs may be applicable for PMI estimation, we did not propose a direct method to achieve this. To date, based on our knowledge, there is one example in the literature proposing a predictive model based on features extracted from PMCT images. Klontzas et al. [51] developed a ML model combining features extracted from the pancreas and the liver and reported promising results demonstrating the feasibility of this approach. The study was based on cross-sectional data in which a single scan was available for each analysed subject.

Table 3 Previously reported significant features. Same as Table 2 but reporting the results for the features found significant in previous works [54, 55]

Name	Feature Class	Model Variant	*p*-val	Log-like	Cond R^2	Fixed Eff	Std Err
Mean	1st Lev. Stat.	Log	6.22E-07	−158.16	0.97	2.53E+00	3.73E-01
Volume	Shape-Based	Log	3.17E-05	−655.38	0.97	−4.29E+03	7.55E+02

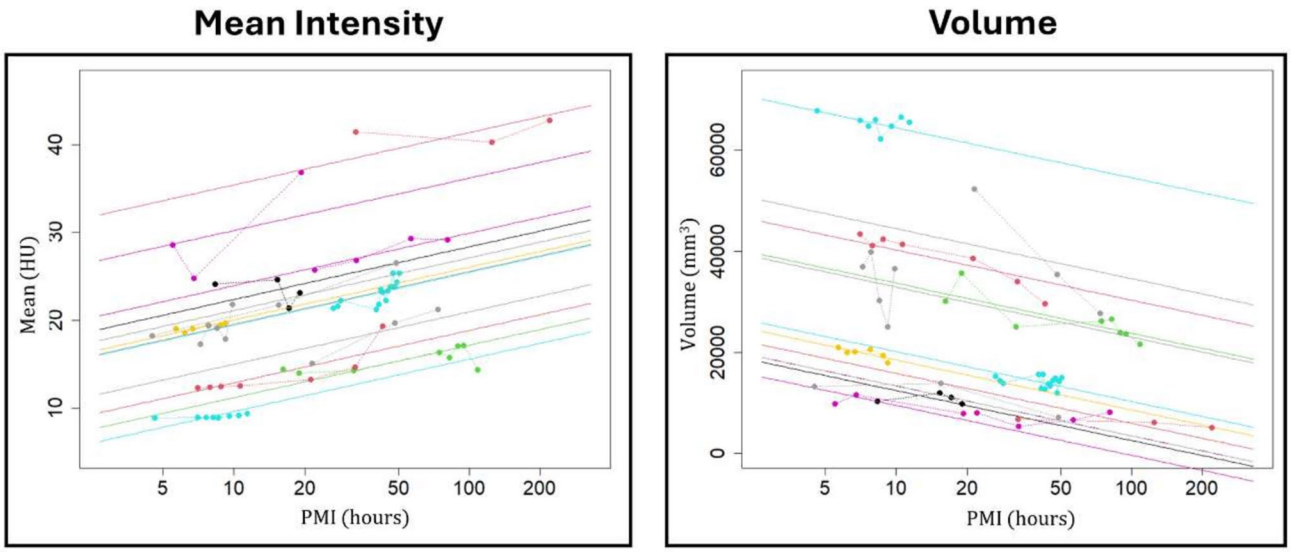

Fig. 3 Previously reported radiomic feature trends. Figure 3 is similar to Fig. 2, but reports the mean values of the lateral cerebral ventricles (LCVs) intensities and their volumes as a function of the postmortem interval (PMI). The two features have been previously reported to be associated with the PMI [54, 55]. We fitted the data with the logarithmic model variant. A logarithmic scale was used on the x-axis

Therefore, this approach allows to predict the PMI given a single unseen scan.

The data available in this study were sequential scans, also known as longitudinal data, i.e. multiple scans acquired at different PMIs for each subject. Compared to cross-sectional data, longitudinal data provides insights into changes over time within the same subjects, allowing for the analysis of temporal patterns and causality, which cross-sectional data cannot achieve. However, this type of data cannot be straightforwardly used to construct predictive models such the one proposed by Klontzas et al. [51]. Nonetheless, this time-based perspective is extremely relevant as it enhances the understanding of individual trajectories, potentially unrevealing the effects of interventions or exposures. Furthermore, this type of studies has the potential of establishing a set of features that are more sensitive to changes, and that could be used in the design of predictive models such the one proposed by Klontzas et al.

This study employed rigorous protocols for PMCT image acquisition; the use of standardized imaging acquisition protocols in future studies might further enhance the reproducibility of radiomics biomarkers. Standardized protocols would ensure that the identified radiomic features are consistently applicable across different platforms and forensic contexts, facilitating broader implementation and validation.

One of the limitations of the study is the assumption that all the subjects share the same rate of feature variation with PMI, i.e. the identification of the slope as a fixed effect. This choice was mainly due to the relatively small size of the dataset. Including the slope as random effect would have most likely led to an overfitting of the data. A wider cohort and a denser sample acquisition in terms of time points could be used to fit more complex models. A subject specific slope could be used to study the association of specific feature changes with particular body conditions or clinical information.

Conclusions

This study presents a quantitative analysis of postmortem modifications in LCVs detectable via PMCT assessment, based on the extraction of radiomic features. We showed that several features are strongly associated with the changes occurring after death, suggesting that these features have the potential to give relevant information for PMI estimation. The use of a radiomic-based analysis in this framework has

several advantages: the quantitative nature of the approach provides a more objective and precise assessment compared to traditional visual examination, reducing subjective bias and improving the reliability of PMI estimation; furthermore, radiomics can detect subtle textural and structural changes in tissues occurring after death, which might be imperceptible to the naked eye; the wide range of features extracted (shape, intensity, texture) provides a comprehensive profile of postmortem changes. This richness of data can help capture various aspects of decomposition, leading to a more robust PMI model; finally, radiomics protocols can be standardized, ensuring consistent and reproducible results across different studies and settings. This consistency is crucial for reliable PMI estimation. This study highlights the potential of PMCT-based radiomics as a source of complementary information that can be integrated into existing methods for estimating PMI. Our results support the application of quantitative imaging approaches in forensic investigations, suggesting that incorporating radiomics could enhance the accuracy and reliability of postmortem interval estimations.

Author contributions All authors contributed to the study's conception and design. Guarantors of integrity of entire study: F.D.G., M.G., L.B., R.G., N.D., E.B., G.F., L.N., V.L.P.; study concepts/study design or data acquisition or data analysis/interpretation, all authors; manuscript drafting or manuscript revision for important intellectual content, all authors; approval of final version of submitted manuscript: all authors; literature research: F.D.G., M.G., L.B., E.B., G.F., V.L.P.; experimental studies: F.D.G., M.G., L.B., R.G., N.D., E.B., G.F.; statistical analysis: M.G., R.G.; and manuscript editing: all authors. All authors read and approved the final manuscript.

Funding This work has been supported by Fondi di Ateneo, Linea D1—Università Cattolica del Sacro Cuore, grant no. R4124500826 to F.D.G.

Declarations

Ethics approval The study was conducted in accordance with the principles of the Helsinki Declaration and was approved by the Institutional Research Ethics Committee of the Catholic University of Rome(ID 3862).

Human Ethics Statements and Consent to Participate Not applicable.

Consent to participate and consent for publication Not needed.

Conflict of interest The authors declare no competinginterests.

References

1. Henssge C, Madea B (2004) Estimation of the time since death in the early post-mortem period. Forensic Sci Int 144(2–3):167–175. https://doi.org/10.1016/j.forsciint.2004.04.051
2. Madea B (2016) Methods for determining time of death. Forensic Sci Med Pathol 12(4):451–485. https://doi.org/10.1007/s12024-016-9776-y
3. Gaudry E, Blais C, Maria A et al (2006) study of steroidogenesis in pupae of the forensically important blow fly Protophormia terraenovae (Robineau-Desvoidy) (Diptera: Calliphoridae). Forensic Sci Int 160(1):27–34. https://doi.org/10.1016/j.forsciint.2005.06.014
4. Zhou C, Byard RW (2011) Factors and processes causing accelerated decomposition in human cadavers - an overview. J Forensic Leg Med 18(1):6–9. https://doi.org/10.1016/j.jflm.2010.10.003
5. Rainy H (1869) On the cooling of dead bodies as indicating the length of time that has elapsed since death. Glasgow Med J 1(3):323–330
6. Brown A, Marshall TK (1974) body temperature as a means of estimating the time of death. Forensic Sci 4(2):125–133. https://doi.org/10.1016/0300-9432(74)90093-4
7. Bate-Smith EC, Bendall JR (1947) Rigor mortis and adenosinetriphosphate. J Physiol 106(2):177–185
8. Bate-Smith EC, Bendall JR (1949) Factors determining the time course of rigor mortis. J Physiol 110(1–2):47–65. https://doi.org/10.1113/jphysiol.1949.sp004420
9. Madea B (1992) Estimating time of death from measurement of the electrical excitability of skeletal muscle. J Forensic Sci Soc 32(2):117–129. https://doi.org/10.1016/s0015-7368(92)73061-8
10. Cordeiro C, Ordóñez-Mayán L, Lendoiro E et al (2019) a reliable method for estimating the postmortem interval from the biochemistry of the vitreous humor, temperature and body weight. Forensic Sci Int 295:157–168. https://doi.org/10.1016/j.forsciint.2018.12.007
11. Henssge C (1988) Death time estimation in case work. I. The rectal temperature time of death nomogram. Forensic Sci Int 38(3–4):209–236. https://doi.org/10.1016/0379-0738(88)90168-5
12. Henssge C, Madea B, Gallenkemper E (1988) Death time estimation in case work. II. Integration of different methods. Forensic Sci Int 39(1):77–87. https://doi.org/10.1016/0379-0738(88)90120-x
13. Pittner S, Bugelli V, Weitgasser K et al. 2020 a field study to evaluate PMI estimation methods for advanced decomposition stages. Int J Legal Med 134(4), 1361–1373. https://doi.org/10.1007/s00414-020-02278-0
14. Henssge C, Madea B, Gallenkemper E (1985) [Determination of the time of death–integration of various partial methods]. Z Rechtsmed 95(3):185–196. https://doi.org/10.1007/bf00201077
15. Henssge C, Althaus L, Bolt J et al (2000) xperiences with a compound method for estimating the time since death. I. rectal temperature nomogram for time since death. Int J Legal Med 113(6):303–319. https://doi.org/10.1007/s004149900089
16. Henssge C, Althaus L, Bolt J et al (2000) xperiences with a compound method for estimating the time since death. II. Integration of non-temperature-based methods. Int J Legal Med 113(6):320–331. https://doi.org/10.1007/s004149900090
17. Thakral S, Purohit P, Mishra R et al (2023) The impact of RNA stability and degradation in different tissues to the determination of post-mortem interval: a systematic review. Forensic Sci Int 349:111772. https://doi.org/10.1016/j.forsciint.2023.111772
18. Singh P, Ali W, Sandhu S et al (2023) Post-mortem interval estimation using miRNAs of road traffic accident cases: a forensic molecular approach. Sci Justice 63(4):485–492. https://doi.org/10.1016/j.scijus.2023.04.011
19. Locci E, Stocchero M, Gottardo R et al (2023) PMI estimation through metabolomics and potassium analysis on animal vitreous humour. Int J Legal Med 137(3):887–895. https://doi.org/10.1007/s00414-023-02975-6

20. Choi KM, Zissler A, Kim E et al (2019) Postmortem proteomics to discover biomarkers for forensic PMI estimation. Int J Legal Med 133(3):899–908. https://doi.org/10.1007/s00414-019-02011-6
21. Brockbals L, Garrett-Rickman S, Fu S et al (2023) Estimating the time of human decomposition based on skeletal muscle biopsy samples utilizing an untargeted LC-MS/MS-based proteomics approach. Anal Bioanal Chem. https://doi.org/10.1007/s00216-023-04822-4
22. Brogdon BG (2000) Scope of forensic radiology. Crit Rev Diagn Imaging 41(1):43–67
23. Eckert WG, Garland N (1984) The history of the forensic applications in radiology. Am J Forensic Med Pathol 5(1):53–56. https://doi.org/10.1097/00000433-198403000-00010
24. Krantz P, Holtås S (1983) Postmortem computed tomography in a diving fatality. J Comput Assist Tomogr 7(1):132–134. https://doi.org/10.1097/00004728-198302000-00024
25. Donchin Y, Rivkind AI, Bar-Ziv J et al. 1994 utility of postmortem computed tomography in trauma victims. J Trauma 37(4), 552–555 discussion 5–6.https://doi.org/10.1097/00005373-199410000-00006
26. Thali MJ, Yen K, Schweitzer W et al (2003) Virtopsy, a new imaging horizon in forensic pathology: virtual autopsy by postmortem multislice computed tomography (MSCT) and magnetic resonance imaging (MRI)–a feasibility study. J Forensic Sci 48(2):386–403
27. Blokker BM, Wagensveld IM, Weustink AC et al (2016) Non-invasive or minimally invasive autopsy compared to conventional autopsy of suspected natural deaths in adults: a systematic review. Eur Radiol 26(4):1159–1179. https://doi.org/10.1007/s00330-015-3908-8
28. Christe A, Flach P, Ross S et al (2010) Clinical radiology and postmortem imaging (Virtopsy) are not the same: specific and unspecific postmortem signs. Leg Med (Tokyo) 12(5):215–222. https://doi.org/10.1016/j.legalmed.2010.05.005
29. Levy AD, Harcke HT, Mallak CT (2010) Postmortem imaging: MDCT features of postmortem change and decomposition. Am J Forensic Med Pathol 31(1):12–17. https://doi.org/10.1097/PAF.0b013e3181c65e1a
30. Okuma H, Gonoi W, Ishida M et al (2014) Comparison of attenuation of striated muscle between postmortem and antemortem computed tomography: results of a longitudinal study. PLoS ONE 9(11):e111457. https://doi.org/10.1371/journal.pone.0111457
31. Shiotani S, Kohno M, Ohashi N et al (2002) Postmortem intravascular high-density fluid level (hypostasis): CT findings. J Comput Assist Tomogr 26(6):892–893. https://doi.org/10.1097/00004728-200211000-00006
32. Lambin P, Rios-Velazquez E, Leijenaar R et al (2012) Radiomics: extracting more information from medical images using advanced feature analysis. Eur J Cancer 48(4):441–446. https://doi.org/10.1016/j.ejca.2011.11.036
33. Gillies RJ, Kinahan PE, Hricak H (2016) Radiomics: images are more than pictures, they are data. Radiology 278(2):563–577. https://doi.org/10.1148/radiol.2015151169
34. Sun R, Limkin EJ, Vakalopoulou M et al. 2018 a radiomics approach to assess tumour-infiltrating CD8 cells and response to anti-PD-1 or anti-PD-L1 immunotherapy: an imaging biomarker, retrospective multicohort study. Lancet Oncol 19(9), 1180–1191. https://doi.org/10.1016/s1470-2045(18)30413-3
35. Morland D, Triumbari EKA, Boldrini L et al (2022) Radiomics in Oncological PET Imaging: a systematic review-part 2, Infradiaphragmatic Cancers, blood malignancies, Melanoma and Musculoskeletal cancers. Diagnostics (Basel) 12(6). https://doi.org/10.3390/diagnostics12061330
36. Morland D, Triumbari EKA, Boldrini L et al (2022) Radiomics in Oncological PET Imaging: a systematic review-part 1, supradiaphragmatic cancers. Diagnostics (Basel) 12(6). https://doi.org/10.3390/diagnostics12061329
37. Albano D, Gatta R, Marini M et al (2021) Role of (18)F-FDG PET/CT radiomics features in the differential diagnosis of solitary pulmonary nodules: diagnostic accuracy and comparison between two different PET/CT scanners. J Clin Med 10(21). https://doi.org/10.3390/jcm10215064
38. Gatta R, Depeursinge A, Ratib O et al (2020) ntegrating radiomics into holomics for personalised oncology: from algorithms to bedside. Eur Radiol Exp 4(1):11. https://doi.org/10.1186/s41747-019-0143-0
39. Petrillo A, Fusco R, Di Bernardo E et al (2022) Prediction of breast Cancer histological outcome by Radiomics and Artificial Intelligence Analysis in contrast-enhanced mammography. Cancers (Basel) 14(9). https://doi.org/10.3390/cancers14092132
40. Boldrini L, Lenkowicz J, Orlandini LC et al (2022) Applicability of a pathological complete response magnetic resonance-based radiomics model for locally advanced rectal cancer in intercontinental cohort. Radiat Oncol 17(1):78. https://doi.org/10.1186/s13014-022-02048-9
41. Casà C, Piras A, D'Aviero A et al (2022) The impact of radiomics in diagnosis and staging of pancreatic cancer. Ther Adv Gastrointest Endosc 15:26317745221081596. https://doi.org/10.1177/26317745221081596
42. Di Dio C, Chiloiro G, Cusumano D et al (2021) Fractal-based radiomic approach to tailor the chemotherapy treatment in rectal cancer: a generating hypothesis study. Front Oncol 11:774413. https://doi.org/10.3389/fonc.2021.774413
43. Nardone V, Boldrini L, Grassi R et al (2021) Radiomics in the setting of Neoadjuvant Radiotherapy: a new approach for tailored treatment. Cancers (Basel) 13(14). https://doi.org/10.3390/cancers13143590
44. Calandrelli R, Boldrini L, Tran HE et al (2022) CT-based radiomics modeling for skull dysmorphology severity and surgical outcome prediction in children with isolated sagittal synostosis: a hypothesis-generating study. Radiol Med 127(6):616–626. https://doi.org/10.1007/s11547-022-01493-6
45. Barnes H, Humphries SM, George PM et al (2023) Machine learning in radiology: the new frontier in interstitial lung diseases. Lancet Digit Health 5(1):e41–e50. https://doi.org/10.1016/s2589-7500(22)00230-8
46. Liang S, Ma J, Wang G et al (2022) The application of artificial intelligence in the diagnosis and drug resistance prediction of pulmonary tuberculosis. Front Med (Lausanne) 9:935080. https://doi.org/10.3389/fmed.2022.935080
47. Giacobbe G, Granata V, Trovato P et al (2023) Gender medicine in clinical radiology practice. J Pers Med 13(2). https://doi.org/10.3390/jpm13020223
48. Xiao F, Sun R, Sun W et al (2022) rediction of potential severe coronavirus disease 2019 patients based on CT radiomics: a retrospective study. Med Phys 49(9):5886–5898. https://doi.org/10.1002/mp.15841
49. De-Giorgio F, Boldrini L (2021) Advanced forensic bioimaging analysis: the radiomics perspective. Forensic Sci Internationa: Rep 4:100247
50. De-Giorgio F, Ciasca G, Fecondo G et al (2022) Post mortem computed tomography meets radiomics: a case series on fractal analysis of post mortem changes in the brain. Int J Legal Med 136(3):719–727. https://doi.org/10.1007/s00414-022-02801-5
51. Klontzas ME, Leventis D, Spanakis K et al (2023) Post-mortem CT radiomics for the prediction of time since death. Eur Radiol. https://doi.org/10.1007/s00330-023-09746-2
52. Zwanenburg A, Vallières M, Abdalah MA et al (2020) The image biomarker standardization initiative: standardized quantitative radiomics for high-throughput Image-based phenotyping.

Radiology 295(2):328–338. https://doi.org/10.1148/radiol.2020191145
53. Tschui J, Jackowski C, Schwendener N et al (2016) ost-mortem CT and MR brain imaging of putrefied corpses. Int J Legal Med 130(4):1061–1068. https://doi.org/10.1007/s00414-016-1385-5
54. Hasegawa I, Shimizu A, Saito A et al (2016) valuation of post-mortem lateral cerebral ventricle changes using sequential scans during post-mortem computed tomography. Int J Legal Med 130(5):1323–1328. https://doi.org/10.1007/s00414-016-1327-2
55. De-Giorgio F, Ciasca G, Fecondo G et al (2021) stimation of the time of death by measuring the variation of lateral cerebral ventricle volume and cerebrospinal fluid radiodensity using postmortem computed tomography. Int J Legal Med 135(6):2615–2623. https://doi.org/10.1007/s00414-021-02698-6
56. Fedorov A, Beichel R, Kalpathy-Cramer J et al (2012) 3D slicer as an image computing platform for the quantitative maging network. Magn Reson Imaging 30(9):1323–1341. https://doi.org/10.1016/j.mri.2012.05.001
57. Dinapoli N, Alitto AR, Vallati M et al. (2015) Moddicom: a complete and easily accessible library for prognostic evaluations relying on image features. Annu Int Conf IEEE Eng Med Biol Soc 771–774.https://doi.org/10.1109/embc.2015.7318476